APPLIED PHYSICS

# A general approach for hysteresis-free, operationally stable metal halide perovskite field-effect transistors

Copyright © 2020 The Authors, some rights reserved; exclusive licensee American Association for the Advancement of Science. No claim to original U.S. Government Works. Distributed under a Creative Commons Attribution NonCommercial License 4.0 (CC BY-NC).

**Satyaprasad P. Senanayak[1,2], Mojtaba Abdi-Jalebi[1,3], Varun S. Kamboj[1], Remington Carey[1], Ravichandran Shivanna[1], Tian Tian[4,5], Guillaume Schweicher[1], Junzhan Wang[1], Nadja Giesbrecht[6], Daniele Di Nuzzo[1], Harvey E. Beere[1], Pablo Docampo[6,7], David A. Ritchie[1,8], David Fairen-Jimenez[4], Richard H. Friend[1], Henning Sirringhaus[1]***

**Despite sustained research, application of lead halide perovskites in field-effect transistors (FETs) has substantial concerns in terms of operational instabilities and hysteresis effects which are linked to its ionic nature. Here, we investigate the mechanism behind these instabilities and demonstrate an effective route to suppress them to realize high-performance perovskite FETs with low hysteresis, high threshold voltage stability ($\Delta V_t$ < 2 V over 10 hours of continuous operation), and high mobility values >1 $cm^2/V{\cdot}s$ at room temperature. We show that multiple cation incorporation using strain-relieving cations like Cs and cations such as Rb, which act as passivation/crystallization modifying agents, is an effective strategy for reducing vacancy concentration and ion migration in perovskite FETs. Furthermore, we demonstrate that treatment of perovskite films with positive azeotrope solvents that act as Lewis bases (acids) enables a further reduction in defect density and substantial improvement in performance and stability of n-type (p-type) perovskite devices.**

## INTRODUCTION

Hybrid organic-inorganic lead halide perovskites (like $CH_3NH_3PbI_3$; hereafter $MAPbI_3$) are a very promising and intensively researched class of semiconductor materials for next-generation high-performance optoelectronic devices that could potentially outperform conventional inorganic devices. Perovskite solar cells with certified power conversion efficiencies reaching up to 24.3% as well as light-emitting diodes (LEDs) with external quantum efficiencies exceeding 20% (*1*–*3*) have been demonstrated. Rapid progress has been enabled by the outstanding optoelectronic properties of lead halide perovskites, such as the long charge carrier diffusion length (*4*), low effective mass of the charge carriers (*5*), and clean band structure (*6*). Consistent improvements of device performance and stability have been achieved by engineering of the interfaces (*7*, *8*), developing perovskite composites with different semiconductors (*9*–*11*), use of carrier selective layers (*12*, *13*), as well as the use of multicationic mixtures (*14*) and incorporation of low-dimensional perovskite structures (*15*, *16*). Despite the remarkable, rapid advances in optoelectronic devices like photovoltaics, LEDs (*17*), and optically pumped lasers (*18*), the fabrication of perovskite field-effect transistors (FETs) has remained challenging (*19*). This is because ion migration in these ionic materials causes a partial screening of the applied gate field, yielding reduced gate modulation of electronic charges at room temperature and reduced field-effect mobilities, $\mu_{FET}$, of typically $10^{-3}$ to $10^{-4}$ $cm^2/V{\cdot}s$ in thin films or single crystals of $MAPbI_3$ (*20*–*23*). For photovoltaic and LEDs, ion migration also leads to a screening of the applied electric field in the semiconductor, but this does not substantially degrade the device performance as currents can be driven by diffusion through the semiconductor. The issue of ionic defect migration in $MAPbI_3$ perovskite FETs has been mitigated to some extent by operating the devices at low temperature wherein the ions are frozen or by using single crystals with low defect densities (*24*). Usage of lead acetate precursor for fabricating $MAPbI_3$ thin films and modifications of the source-drain contacts with suitable interfacial layers have previously been shown to be effective to achieve reasonable FET characteristics from 100 to 300 K with a $\mu_{FET}$ of 0.5 $cm^2/V{\cdot}s$ at room temperature (*25*). Despite these advances, $MAPbI_3$ FETs still exhibit nonideal transistor characteristics with large hysteresis and a high degree of bias stress–induced instability and large threshold voltage shifts upon continuous operation (*25*, *26*). Hence, for perovskite FETs to become more useful, both for fundamental transport studies and for potential applications, there is a need to develop approaches to improve their performance and long-term operational stability and achieve hysteresis-free gate modulation.

Incorporation of multication mixtures such as formamidinium [FA; $HC(NH_2)_2^+$] or Cs or Rb, which either replace the methylammonium (MA) cation or act as passivation agents, has been shown to increase stability and reduce hysteresis in photovoltaic devices (*14*, *27*). However, the molecular origin of stability in these multicationic perovskites remains incompletely understood. Here, we use FETs as a platform to investigate the molecular mechanism for the operational stability and hysteresis characteristics of multication perovskite optoelectronic devices. Triple-cation $Cs_x(MA_{0.17}FA_{0.83})_{1-x}Pb(Br_{0.17}I_{0.83})_3$ has been previously investigated, and balanced ambipolar characteristics with field-effect mobilities of 2 $cm^2/V{\cdot}s$ at room temperature were reported (*28*); however, the hysteresis and stability were not studied. In the present work, we perform a systematic investigation of performance and operational stability of multication perovskite FETs and identify an effective strategy to suppress vacancy formation and ion migration in these materials through the use of Lewis base and acid treatments for n-type and p-type perovskite semiconductors,

[1]Cavendish Laboratory, University of Cambridge, JJ Thomson Avenue, Cambridge CB3 0HE, UK. [2]CSIR- Institute of Minerals and Materials Technology Council of Scientific & Industrial Research, Bhubaneswar–751 013, Odisha, India. [3]Institute for Materials Discovery, University College London, Torrington Place, London WC1E 7JE, UK. [4]Adsorption and Advanced Materials (AAM) Laboratory, Department of Chemical Engineering and Biotechnology, University of Cambridge, Philippa Fawcett Drive, Cambridge CB3 0AS, UK. [5]Department of Chemical Engineering, Imperial College London, South Kensington Campus, London SW7 2AZ, UK. [6]Department Chemie, Ludwig-Maximilians-Universität-München, Butenandtstr, München, Germany. [7]School of Mathematics, Statistics and Physics, Newcastle University, Herschel Building, Newcastle upon Tyne NE1 7RU, UK. [8]Department of Physics, Swansea University, Sketty, Swansea SA2 8PQ, UK.
*Corresponding author. Email: hs220@cam.ac.uk



Downloaded from http://advances.sciencemag.org/ on April 10, 2020

respectively. We demonstrate high-performance, hysteresis-free perovskite FETs with mobilities >1 $cm^2/V \cdot s$ and operational stability comparable to that of other established FET technologies. Using electrical, spectroscopic, and structural characterization, we identify potential mechanisms for the suppression of ion migration in multication compositions and acid/base treatments.

## RESULTS

### Optimization of multication perovskite FETs

The choice of the perovskite precursor material and the technique for solution deposition significantly affects the charge transport behavior in perovskites. We showed previously that the use of $Pb(Ac)_2$ precursor improves the performance of bottom-contact, top-gate $MAPbI_3$ FETs (*25*), while devices fabricated with $PbI_2$ precursor exhibit much poorer performance in the same device architecture (*19*, *20*). We use here the same bottom-contact, top-gate FET architecture with gold source-drain contacts and a Cytop gate dielectric layer as in (*29*). Unfortunately, because of solubility constraints, the use of $Pb(Ac)_2$ precursor severely limits the incorporation of multication mixtures, such as FA, Cs, or passivation agents (e.g., Rb, K) into $MAPbI_3$. Hence, we first sought to optimize the conventional $PbI_2$ precursor–based $MAPbI_3$ perovskite thin-film fabrication through the antisolvent technique (Materials and Methods and section S1). In Fig. 1, we show the device characteristics of n-type, top-gate perovskite FETs fabricated with the antisolvent method and different cation compositions. $MAPbI_3$ FETs made from $PbI_2$ precursor with antisolvent (Fig. 1A) exhibit at least an order of magnitude increase in the channel current compared to devices fabricated without the antisolvent technique (fig. S1A) and are comparable to devices fabricated with $Pb(Ac)_2$ precursor (fig. S1, C and D). However, despite extensive optimization, the devices still exhibit notable hysteresis, evident in the transfer characteristics of Fig. 1A, but particularly in the output characteristics at 300 K (fig. S2), which bear the signature of ion migration under the action of the applied gate and source-drain electric fields. Moreover, the output characteristics, particularly of devices with relatively small channel length ($L$ = 20 μm), exhibit sizable contact resistance, as evidenced by a suppression of the current at small source-drain voltages. Using the transfer line method in the linear regime of the output characteristics (forward sweep), the contact resistance was estimated to be as low as (400 ± 70) kilohm·cm at 300 K in the best devices, but we observed significant variations from batch to batch (fig. S3). To minimize the contact resistance, most devices discussed in the following were fabricated with a long channel length of 100 μm. $MAPbI_3$ FETs fabricated with $L$ = 100 μm exhibit some improvement in the hysteretic performance at both 100 and 300 K compared to devices fabricated with $L$ = 20 μm (Fig. 1B and fig. S2).

Nevertheless, despite extensive optimization, $MAPbI_3$ FETs retain sizable hysteresis and nonidealities that make them poorly suitable for both fundamental transport studies and applications and necessitate the exploration of more complex compositions. At 100 K, where ionic defect migration is negligible, the hysteresis can be attributed to the strong dipolar nature of the MA cation ($MA^+$).

Downloaded from http://advances.sciencemag.org/ on April 10, 2020

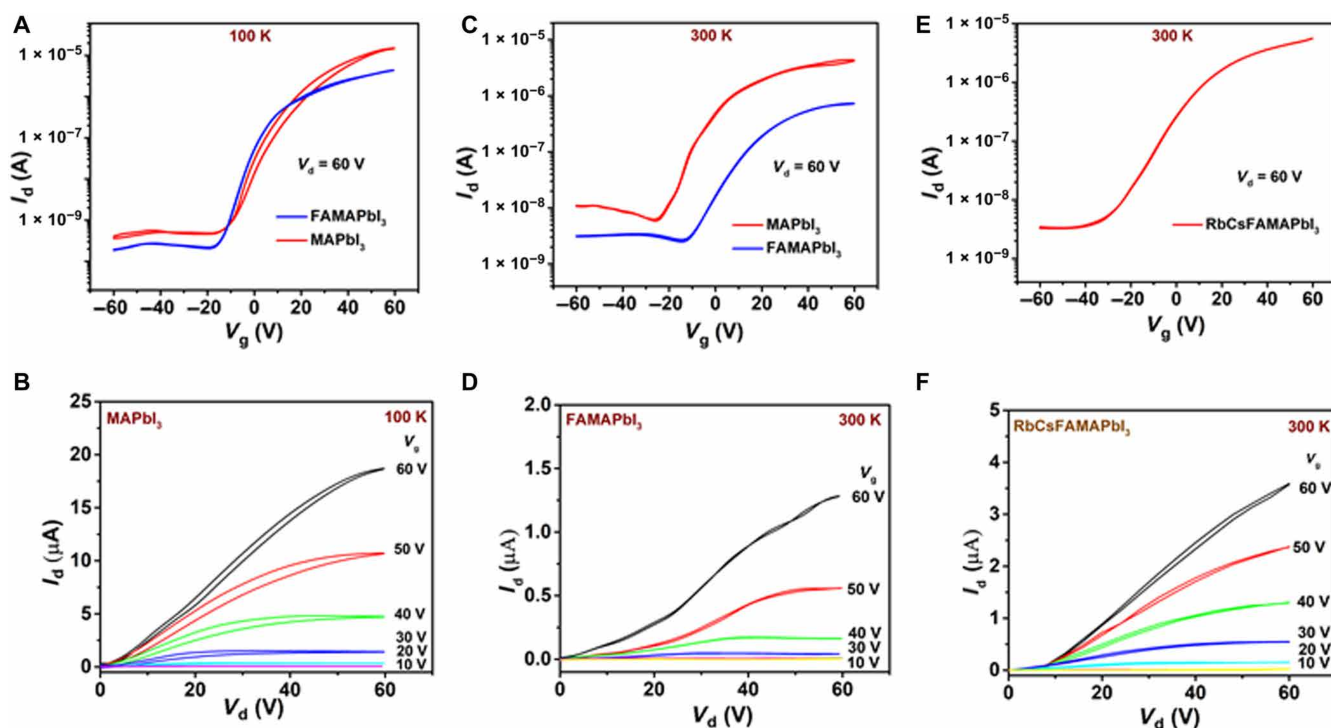


**Fig. 1. Top-gate perovskite FETs fabricated by the antisolvent method—effect of channel length and cation composition.** (**A**) Transfer characteristics measured at 100 K on top-gate, bottom-contact perovskite FET fabricated from $MAPbI_3$ (red) and $FAMAPbI_3$ (blue) with $L$ = 100 μm, $W$ = 1 mm. (**B**) Output characteristics measured on the same $MAPbI_3$ FET depicting a decrease in hysteresis compared to devices fabricated with $L$ = 20 μm, $W$ = 1 mm (figs. S1A and S2A). Transfer characteristics measured at 300 K on perovskite FET ($L$ = 100 μm, $W$ = 1 mm) fabricated from (**C**) $MAPbI_3$ (red) and $FAMAPbI_3$ (blue). (**D**) Corresponding output characteristics measured on $FAMAPbI_3$ perovskite FETs with $L$ = 100 μm, $W$ = 1 mm. (**E**) Enhancement in the ON current in the transfer characteristics for FETs ($L$ = 100 μm, $W$ = 1 mm) fabricated with $RbCsFAMAPbI_3$; the corresponding output characteristics (**F**) exhibit low hysteresis, but there is still some suppression of the current at small drain voltages, indicating sizable contact resistance.

As the effective electric field along the channel decreases with increased channel length, the polarization of the cation decreases, and this manifests in the observed reduction in hysteresis at 100 K with longer channel length. Similar behavior is observed when $MA^+$ is replaced by $FA^+$ (*30*). Bottom-contact, top-gate $FAPbI_3$ FETs exhibit nearly hysteresis-free transfer and output characteristics at 100 K, even for $L$ = 20 μm (fig. S4). This is consistent with the measured dielectric constant $\varepsilon_r = Cd/\varepsilon_o A$ (where $C$ is the capacitance, $d$ is the film thickness, $A$ is the area of the capacitor, and $\varepsilon_o$ is the vacuum permittivity), which is estimated to be $\varepsilon_r$ ~ 27 (at 100 kHz) for $MAPbI_3$ and decreases to 4.3 (at 100 kHz) for $FAPbI_3$ (fig. S5). Consequently, the expected dipole moments of the $MA^+$ and $FA^+$ cations at room temperature, estimated using the Kirkwood-Fröhlich formalism for polar, orientationally disordered solids, are 1.94 and 0.45 D, respectively (section S2) (*29*, *31*, *32*).

Unfortunately, the hysteresis-free characteristics of $FAPbI_3$ are not retained to room temperature and also the magnitude of the transistor current $I_{ds}$ is lower by up to two orders of magnitude for $FAPbI_3$ than for $MAPbI_3$ at 300 K (fig. S6). This can be attributed to the coexistence of a small fraction (~5.7%) of the nonperovskite δ-$FAPbI_3$ phase along with the perovskite α-$FAPbI_3$ phase, which is evident in the x-ray diffraction (XRD) patterns (fig. S7) and the shape of the optical absorption edge measured by photothermal deflection spectroscopy (PDS) (fig. S8) (*33*). The issue of the nonperovskite yellow phase can be mitigated by introduction of mixed cation compositions of $FA^+$, $MA^+$, and $Cs^+$ while maintaining iodide as the halide ion (section S4) (*27*, *34*). We undertook an optimization of composition and identified $FA_{0.2}MA_{0.8}PbI_3$ (referred to as $FAMAPbI_3$ hereafter) and $Cs_{0.05}FA_{0.17}MA_{0.78}PbI_3$ ($CsFAMAPbI_3$) as optimized compositions, which exhibit nearly hysteresis-free transfer characteristics at 300 K with a $\mu_{FET}$ ~ (0.1 ± 0.03) and ~ (0.3 ± 0.05) $cm^2/V{\cdot}s$, respectively (Fig. 1C and section S5), which is comparable to the best $MAPbI_3$ devices with $\mu_{FET}$ ~ 0.5 $cm^2/V{\cdot}s$. FETs with $L$ = 100 μm fabricated from $FAMAPbI_3$ and $CsFAMAPbI_3$ also exhibited significant improvement in output characteristics measured at 300 K with well-defined linear and saturation regimes (Fig. 1D). We also fabricated devices with more complex compositions, such as $Cs_{0.05}FA_{0.78}MA_{0.17}Pb(I_{0.78}Br_{0.17})_3$, for which high solar cell efficiencies have previously been reported (*27*); these exhibited rather lower $\mu_{FET}$ ~ 0.003 $cm^2/V{\cdot}s$ (fig. S13B). To further enhance FET performance, we also explored Rb passivation by adding RbI solution into the $CsFAMAPbI_3$ precursor solution in varying compositions (1, 5, and 10%). Upon the addition of RbI, we observed an increase in the channel current and $\mu_{FET}$ reached a value of ~0.8 $cm^2/V{\cdot}s$ in best devices for a 5% concentration of Rb in solution (referred to as $RbCsFAMAPbI_3$ hereafter) (Fig. 1E). Further increasing the Rb concentration to 10%, $\mu_{FET}$ drops down to ~0.001 $cm^2/V{\cdot}s$ (fig. S14A), which is consistent with the observation of a phase-segregated, Rb-based nonperovskite phase in both XRD and SEM (section S4) (*35*). Similar enhancement in charge carrier mobility upon the addition of Rb to $CsFAMAPbI_3$ has also been observed through microwave conductivity and time-of-flight measurements (*36*). The output characteristics measured on Rb-passivated devices exhibited even cleaner, hysteresis-free output characteristics (Fig. 1F). We also explored potassium passivation for $CsFAMAPbI_3$, which has been shown to inhibit ionic migration and remove hysteresis in solar cells, but this resulted in poor $\mu_{FET}$ ~ $10^{-4}$ $cm^2/V{\cdot}s$ and loss of gate modulation upon increasing the K composition to 10%. We attribute this behavior to the formation of a segregated, nonconducting KI ionic solid phase, which screens the gate potential (fig. S14B) (*37*). Nevertheless, from these wide compositional variations, we understand that even a small variation of 1 to 2% of specific cations is enough to drastically degrade the FET performance. This behavior can be related to a number of factors like the propensity to phase segregation as well as disorder energetics and the overall stability of the crystal structure (as shown in the later sections).

### Ionic defect dynamics

To directly probe ion migration at 300 K in these devices, we monitored the temporal variation of the channel current and the optical properties of the channel while the perovskite FET is operated continuously in the transdiode mode ($V_d = V_g$ = 60 V) (Fig. 2). The $I_{ds}(t)$ characteristics of $MAPbI_3$ devices (Fig. 2A) exhibit a complex behavior for the first tens of seconds that depends on channel length, but at later times, a rise in the current is observed, which sets in the earlier for devices with shorter channel lengths. This rise in the current is attributed to lateral ionic defect migration resulting in healing of iodine vacancies and/or decrease in the contact resistance when ions start to accumulate at the metal-semiconductor interface (*38*, *39*). After prolonged biasing (>100 to 1000 s), the current is observed to decrease. This potentially reflects processes involving electrochemical degradation of the electrodes. The characteristic time scale for ion/defect migration can be estimated from the intersection of linear fits of the early time behavior and the current rise (as indicated in Fig. 2A). The characteristic time scale for the onset of ionic migration ($\tau_c$) is observed to change from 8 s for FETs with $L$ = 20 μm to 38 s for FETs with $L$ = 100 μm (Fig. 2B). Using a simplistic time-of-flight estimation, the mobility of the ions can be estimated as $5 \times 10^{-7}$ $cm^2/V{\cdot}s$, which is comparable to the reported values for iodine migration in $MAPbI_3$ (*39*, *40*). This behavior correlates well with the observed improved performance of long channel devices and also the observation that the extracted temperature-dependent mobility $\mu_{FET}$(T) decreases more rapidly with increasing temperature for small $L$ (fig. S15). In $FAMAPbI_3$ and $CsFAMAPbI_3$ devices, $\tau_c$ increases to 72 and 226 s, and for Rb-passivated $CsFAMAPbI_3$, the current remains stable for $10^3$ s, indicating a much improved stability toward ionic/defect migration by the addition of Rb (Fig. 2C). This is fully consistent with the absence of hysteresis in the FET characteristics.

### Photoluminescence mapping of ionic defects

We also visualized iodine migration by performing photoluminescence (PL) mapping (in nitrogen atmosphere) under bias on lateral devices ($L$ ~ 20 μm). Unbiased devices exhibited uniform PL intensity profile throughout the channel (Fig. 2D). Devices were then poled at $V_d$ = 60 V for 180 s, and PL mapping was performed over the same area. Upon biasing, the PL profiles of $MAPbI_3$ devices exhibit an approximately exponential decay, with the positive electrode exhibiting a lower PL intensity and the negative electrode exhibiting a higher PL intensity (Fig. 2, D to F). This trend is similar to the observation where photo-induced brightening occurs when iodine is depleted and decrease in PL intensity is observed upon accumulation of iodine defect (*39*, *41*). This has been well studied by exposing perovskite films to laser illumination (*41*), voltage bias (*39*), and $I_2$ vapors. Upon increasing the channel length, the characteristic decay length of the PL (after 180 s of biasing) away from the negative electrode decreases (Fig. 2, E and F) from 0.3 × $L$ for 10-μm devices to 11.5 × $L$ for 100-μm devices. Devices fabricated with $RbCsFAMAPbI_3$ thin

Downloaded from http://advances.sciencemag.org/ on April 10, 2020

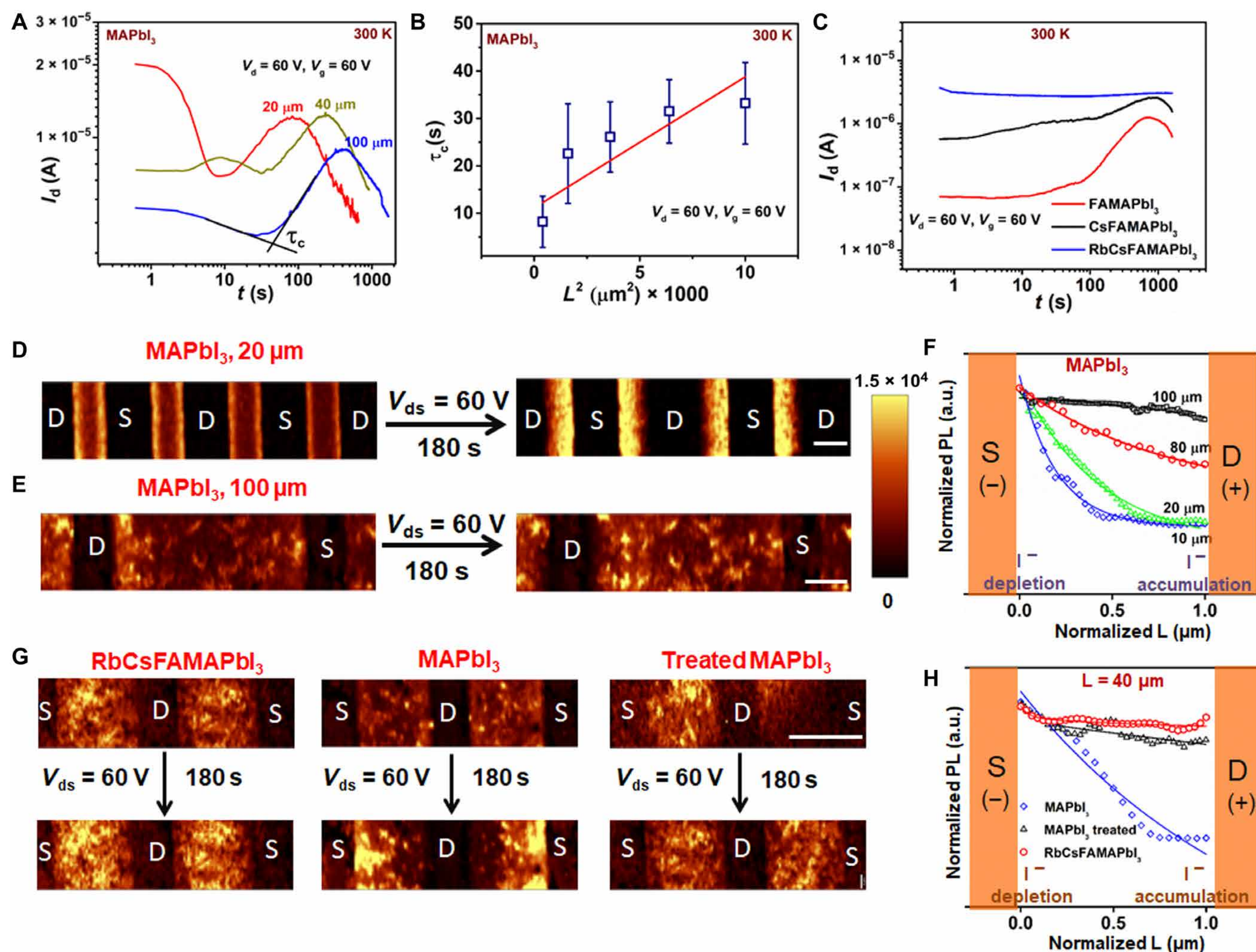


**Fig. 2. Measurements of lateral ion migration as a function of composition.** (**A**) Temporal variation of $I_{ds}$, when a top-gate $MAPbI_3$ transistor fabricated with different $L$ is operated in transdiode mode $V_d = V_g = 60$ V. (**B**) Plot of $\tau_c$ with $L^2$ indicating a typical time-of-flight behavior. (**C**) Similar temporal variation of the $I_{ds}$ measurement performed on top-gate FETs ($L = 100$ μm, $W = 1$ mm) fabricated with $FAMAPbI_3$, $CsFAMAPbI_3$, and $RbCsFAMAPbI_3$ perovskite layers. Photoluminescence (PL) mapping performed on lateral channels of $MAPbI_3$ devices fabricated with different channel lengths (**D**) 20 μm and (**E**) 100 μm before and after application of a source-drain voltage of 60 V for 180 s. (**F**) Line profile of the PL along the channel in $MAPbI_3$ devices with different channel length. Lateral PL mapping measured on (**G**) $RbCsFAMAPbI_3$, $MAPbI_3$, methyl acetate (Lewis base)–treated $MAPbI_3$ devices fabricated with $L = 40$ μm. (**H**) Corresponding PL profiles obtained from the lateral cross section of the different materials in (G) for a channel length of 40 μm. Scale bars, 20 μm (D and E) and 40 μm (G). a.u., arbitrary units.

films exhibited negligible variation in the PL profile even after biasing (at $V_d$ = 60 V for 180 s), providing further evidence for the much reduced ion migration upon Rb passivation (Fig. 2, G and H).

To understand the beneficial effect of multication composition on ion migration, we estimated the vacancy formation energy ($H_f$), which is directly proportional to the latent heat of fusion or decomposition of the crystal ($L_f$), i.e., $H_f = (L_f \times M)/C$, where $M$ is the molar mass of the material and $C$ is a constant, which is dependent on the crystal structure of the material (*42*). We estimated the heat of fusion/melting for the perovskite thin films from dynamic scanning calorimetry. A clear phase transition possibly due to the volatilization of cations and/or residual iodine, which corresponds to the decomposition of the perovskite crystal structure, is observed in all the perovskite thin films, and the decomposition temperature was observed to increase from 191°C for $MAPbI_3$ to 243°C for $RbCsFAMAPbI_3$ thin films (fig. S16). Correspondingly, the enthalpy of fusion/decomposition increases from 11 J/g in $MAPbI_3$ thin films to ~88 J/g in $RbCsFAMAPbI_3$ thin films (table S1). After correcting for the molar mass of the perovskites and assuming the same tetragonal crystal structure, $H_f$ is estimated to increase by a factor of 8 for $RbCsFAMAPbI_3$ compared to $MAPbI_3$, suggesting that the vacancy concentration is indeed expected to be lower in the former.

## Magnetic signatures of ionic defects in perovskites

To obtain a spectroscopic signature of the defects involved in ion migration, we performed electron paramagnetic resonance (EPR) on solid crystalline samples. At room temperature, no EPR signal was detected on any of the compositions, but upon cooling the samples to a temperature <40 K, a well-defined EPR resonance was observed (Fig. 3A). It has a simple, narrow line shape and cannot be attributed to the $MA^+$ cation, which is expected to exhibit a multiple peak shape due to cationic radicals and the interaction of the unpaired electrons

Downloaded from http://advances.sciencemag.org/ on April 10, 2020

with H and N nuclei. Similarly, any iodine-related centers with a nuclear spin of 5/2 are expected to exhibit a hyperfine splitting with six lines (*43*, *44*). Hence, the observed EPR signal can only be attributed to the paramagnetic states of $Pb^{+}$ or $Pb^{3+}$. The observation of an isotropic signal with a $g \sim 2.0007$ points to $6s^1$ electrons of $Pb^{3+}$ as the origin of the EPR since $Pb^{+}$ would be expected to exhibit strongly axial *g* tensors with a *g* value between 1 and 1.7 (*43*, *44*). On the basis of the EPR spectra, the spin density is estimated to be $1.1 \times 10^{14}$ $cm^{-3}$ for $MAPbI_3$ samples; this decreases to $5.2 \times 10^{12}$ $cm^{-3}$ for $RbCsFAMAPbI_3$ (details in Materials and Methods). However, note that the spin density estimated from EPR is too low to directly cause device hysteresis, as this would require the thickness-integrated spin density in our typically 150- to 200-nm-thick perovskite films to be comparable to the FET-induced charge density, which is on the order of $10^{11}$ to $10^{12}$ $cm^{-2}$. This suggests that not all defects causing hysteresis are EPR active. One plausible explanation that has been put forward in the literature is that the $Pb^{3+}$ defects are due to substitution of lattice iodine by oxygen (*44*). This could explain the observed reduction in EPR spin density for the multiple cation compositions, as the density of such oxygen-related defects is likely to be the smaller the lower the iodine vacancy concentration. We also measured the temperature dependence of the magnetic susceptibility ($\chi$) using a superconducting quantum interference device (SQUID) magnetometer (section S8 and fig. S17). From these measurements, we estimate the spin concentration to be $2.1 \times 10^{18}$ $cm^{-3}$ for $MAPbI_3$ samples, which decreases by an order of magnitude to $2 \times 10^{17}$ $cm^{-3}$ for $RbCsFAMAPbI_3$; such spin concentrations are large enough to be directly involved in device hysteresis. This observation provides evidence for a reduction of defect density in multiple cation systems; it is also consistent with our interpretation that the $Pb^{3+}$ defects observed in EPR are merely a fingerprint of iodine vacancies, i.e., originate from vacancy sites that are occupied by oxygen.

## Probing the lattice strain in perovskite with THz spectroscopy

To investigate the charge carrier dynamics and elucidate further the origin of the improved hysteresis, we performed broadband terahertz (THz) time-domain spectroscopy on operating FETs and observed the variation of specific phonon bands under bias. For these measurements, we used a bottom-gate, bottom-contact FET architecture on moderately doped $Si/SiO_2$ wafers. This device architecture was preferred to allow probing of the channel in the transmission geometry since conducting metals used in the top-gate geometry completely absorb the THz radiation and do not permit probing the channel region (details in section S9 and Materials and Methods). Broadband THz spectroscopy on perovskite thin films exhibits three prominent peaks close to 1, 1.8, and 2.8 THz that can be attributed to Pb-I octahedron cage vibrations (details in section S9) (*44*–*46*). Upon biasing $MAPbI_3$ devices in transdiode mode ($V_d$ = 60 V, $V_g$ = 60 V), we observe a broadening of ($\Delta\omega$) ~ 0.08 THz for the lowest-energy 1-THz phonon mode, which is related to octahedron distortion involving a change in I-Pb-I bond angle (Fig. 3, B to D and fig. S18). This broadening of the phonon mode decreases upon substituting with multicationic mixture and is negligible for devices fabricated with $CsFAMAPbI_3$ and $RbCsFAMAPbI_3$ (Fig. 3, B and C and fig. S19). The phonon mode at 2.8 THz, which governs the coupling between the A cation and the Pb-I octahedron cage, exhibits a sharpening of around 10 GHz under bias for $MAPbI_3$ devices; this can be attributed to a

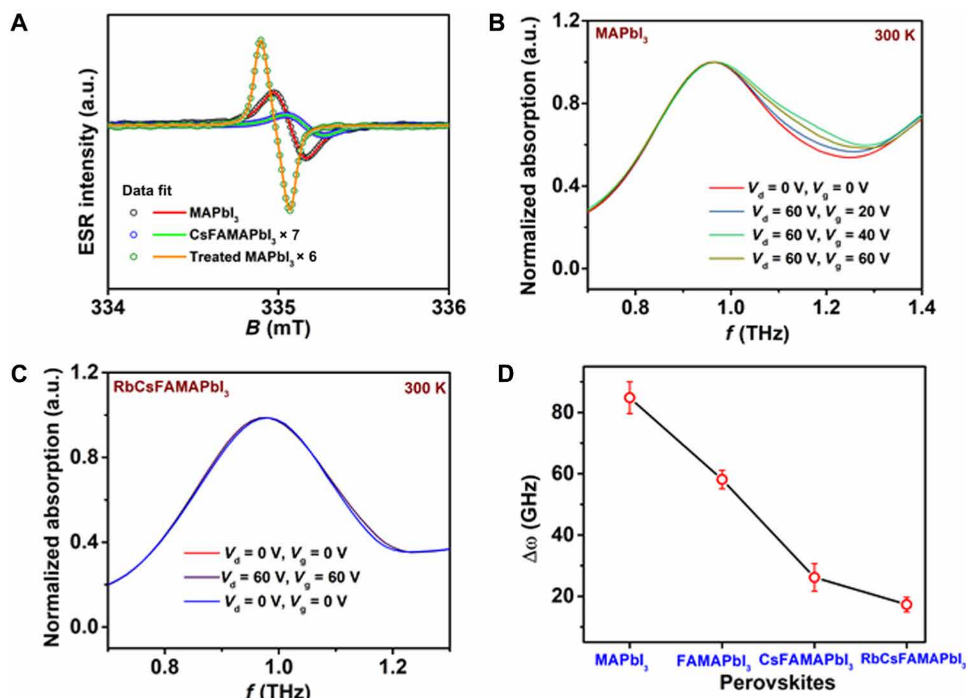


**Fig. 3. Spectroscopic characterization of defect states.** (**A**) Derivative ESR spectra data (scatter) and best fits (line) measurement at 40 K performed on different perovskite samples. Representative THz absorption spectra measured on a bottom contact bottom gate transistor (L = 80 μm, W = 19.5 cm) fabricated using (**B**) $MAPbI_3$ (**C**) $RbCsFAMAPbI_3$, perovskite under different biasing conditions illustrating the broadening of the phonon mode. (**D**) Plot of the bias induced broadening of the first phonon peak around 1 THz in different perovskite materials. Bias-induced broadening is estimated from the difference in the FWHM for THz absorption spectra measured at $V_d = V_g$ = 0V and $V_d = V_g$ = 60V after a Gaussian fit.

Downloaded from http://advances.sciencemag.org/ on April 10, 2020

decrease in entropy of the $MA^+$ cation upon biasing (fig. S21A). No such variation is observed in the phonon mode at 2.6 THz under bias in $FAMAPbI_3$ (fig. S21B). A possible interpretation of the bias-induced broadening at 1 THz is that it reflects the considerable strain in the $MAPbI_3$ lattice that could be released when the injected electrons polarize the I-Pb bond (*46*). Since the energy levels of these perovskites originate from the Pb-6p and I-5p orbital, distortion of the Pb-I octahedron cage under bias modifies the energy landscape for charge transport and could also be a factor in the hysteretic characteristics. Lattice strain originates owing to ionic size mismatch between the A cation and the lead halide cage, and strain relaxation occurs through vacancy formation (*47*). Through the incorporation of smaller cations such as Cs into the lattice, the strain is expected to be reduced (*48*), making the lattice more stable and less susceptible to distortions upon charge injection. The beneficial effect of Rb is unlikely to be directly related to such strain relaxation as Rb has been found not to be directly incorporated into the perovskite lattice; it could be due to changes in crystallization kinetics and improved crystalline quality instead.

## Moisture adsorption in perovskites

Despite the observed enhancement in FET performance with the utilization of Rb-passivated $CsFAMAPbI_3$ perovskite, the output characteristics are still not completely ideal and exhibit injection-limited characteristics (Fig. 1F). Moreover, the best estimated $\mu_{FET} \sim 0.8\ cm^2/Vs$ is lower than the maximum mobility values that could theoretically be achievable in this class of materials, suggesting room for further improvement (*31*). Hence, we considered the role of extrinsic impurities like water and/or oxygen, which are well known to severely degrade charge transport properties in n-type organic semiconductors (*49*–*52*). Adsorbed water is ubiquitous in perovskite FET device fabrication due to the hygroscopic nature of the perovskite precursor and solvents and residual moisture/oxygen in the substrate, dielectric layer, and the nitrogen glove box used for film processing and device testing (*53*). These water molecules get incorporated into pores in the thin films or at grain boundaries and could act as a trap center for electron charge transport (*49*). Typical transfer characteristics obtained on perovskite FETs upon exposure to ambient moisture condition are shown in fig. S22A. To quantify the porosity of the perovskite films, $N_2$ adsorption isotherms at 77 K were measured on perovskite thin films by performing suitable sample degassing (details in Materials and Methods) without any sample degradation. All the samples exhibit type III isotherms, indicating weak adsorbent-adsorbate interaction and the absence of any microporosity, but the presence of a small amount of mesopores. $N_2$ adsorption isotherms exhibited the highest Brunauer-Emmett-Teller (BET) surface area for $MAPbI_3$ thin films, which decreases by half for $RbCsFAMAPbI_3$ (fig. S24, A and B). We also observed a comparable weight loss, which can be attributed to a number of factors like water (*54*), residual solvent, and/or methyl ammonium cation evaporation in thermogravimetric analysis (TGA) measurements at $T = 100°C$; $MAPbI_3$ thin films exhibited a weight loss of 4 to 5% while $RbCsFAMAPbI_3$ thin films exhibited a much smaller weight loss of only 1%. This is consistent with a reduced mesoporosity and BET surface area in $RbCsFAMAPbI_3$ and therefore a reduced susceptibility to water adsorption (fig. S24D). To study the performance of perovskite films in the strict absence of water, we placed a bottom-gate, bottom-contact $MAPbI_3$ device near a strong desiccant cobalt (II) chloride. FETs exposed to $CoCl_2$ exhibited a notable increase in performance (Fig. 4A) with higher ON current and decreased subthreshold swing from 16 to 11 V/dec, indicating a decrease in trap density.

## Azeotropic solvent treatment on perovskite

An alternative technique to reduce the water content in the films, which has recently been found to be very effective for organic semiconductors (*55*), is to wash the top surface of the perovskite film with an orthogonal solvent, which forms a positive azeotrope with water (*56*). Azeotropes are formed when two or more liquids form a constant boiling mixture with a boiling point lower (higher) than that of the constituent liquid, which is referred to as a positive (negative) azeotrope. Before spin coating the top dielectric layer and the gate electrode, we treated $MAPbI_3$ films with the following solvents that form positive azeotropes with water: diethyl ether, methyl acetate, ethyl acetate, pyridine, 1,3,5-trinitrobenzene, and 1,3,5-tribromobenzene. We also investigated the zeotropic solvents, fomblin, and acetic acid that do not suppress the boiling point of water (table S2) (*57*). Devices treated with diethyl ether, which exhibits the lowest boiling point azeotropic mixture of 34°C, exhibited an increase in $I_{ds}$ by two orders of magnitude (Fig. 4B), whereas $MAPbI_3$ devices treated with pyridine with an azeotropic boiling point of 92°C exhibited no improvement in ON current (Fig. 4C) (*56*). We observe a clear correlation between the boiling point lowering of the water-solvent azeotropic mixture and the enhancement in the transistor ON current. The positive azeotrope treatment also leads to a positive shift in the FET turn-on voltage (Fig. 4B) and a decrease in the subthreshold swing (fig. S25); correspondingly, the estimated trap density decreases from $10^{13}$ to $10^{12}\ cm^{-2}\ eV^{-1}$ (details in section S11) (*58*, *59*). This suggests that the positive azeotrope treatment effectively removes water from the films.

However, water removal is not the only factor that governs the efficacy of such solvent treatments. A second key factor appears to be whether the solvent acts as a Lewis acid or a Lewis base: $MAPbI_3$ devices treated with 1,3,5-trinitrobenzene, which has an azeotropic boiling mixture of 98°C but acts as Lewis acid, exhibited a complete loss in gate modulation (fig. S27). In contrast, devices treated with zeotropic acetic acid, which acts as a Lewis base due to the oxygen electron lone pair in the acetate group, exhibited ON current rather similar to that of pristine samples. All the positive azeotropes that were found very effective are able to form Lewis base pairs with unsaturated Pb centers. Unfortunately, it was not possible to find a solvent that forms a negative azeotrope with water, acts a Lewis base, and has a solubility that is sufficiently orthogonal to the perovskite.

A potential explanation for the efficacy of positive azeotrope, Lewis base treatments in improving the performance of these n-type perovskite films is that the process of perovskite film fabrication results in formation of electron trap sites linked to water/oxygen incorporation and potentially to overcoordinated $Pb^{3+}$ species with a net positive charge. This creates a favorable condition for coordination or formation of a dative bond with electron-rich Lewis base solvent molecules, which passivates the overcoordination by donating unpaired electrons (*56*). To investigate this mechanism, we performed solvent treatment on solid samples of $MAPbI_3$ and counted the number of free spins attributed to the $Pb^{3+}$ ions both before and after solvent treatment. Upon treatment with a Lewis base solvent (details in Materials and Methods), the number of paramagnetic $Pb^{3+}$ ions detected in EPR approximately halves to $7 \times 10^{13}\ cm^{-3}$, and the overall paramagnetic defect density extracted from the magnetic susceptibility decreases to $1.3 \times 10^{18}\ cm^{-3}$ (Fig. 3A and fig. S17). In

Downloaded from http://advances.sciencemag.org/ on April 10, 2020

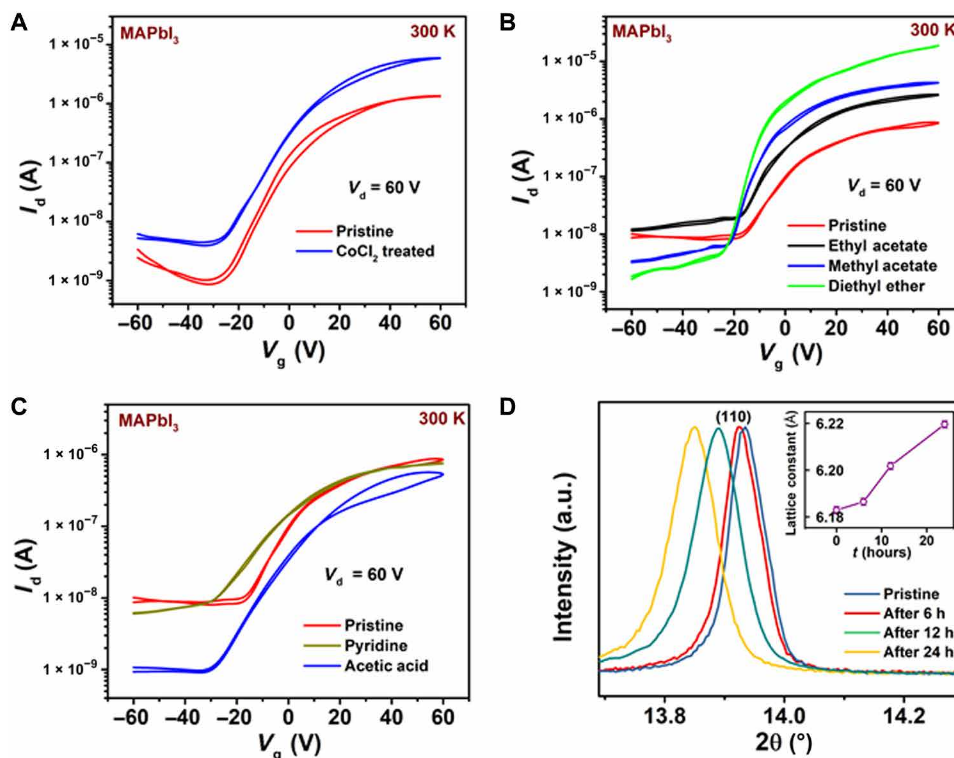


**Fig. 4. Enhancement of $MAPbI_3$ transistor performance with positive azeotrope, Lewis base solvent treatments.** Variation in the transfer characteristics of $MAPbI_3$ perovskite FETs ($L$ = 100 μm, $W$ = 1 mm) (**A**) when exposed to a $CoCl_2$ desiccant layer. Also shown are treatments with a different class of orthogonal solvents: (**B**) Lewis bases (ethyl acetate, methyl acetate, and diethyl ether) that also form a low boiling azeotropic mixture with water and (**C**) Lewis bases (pyridine and acetic acid) that do not form a low boiling azeotropic mixture with water. (**D**) Shift in the XRD peak corresponding to (110) depicting the increase in lattice size upon treatment of $MAPbI_3$ films with methyl acetate solvent. Diethyl ether was avoided because of its low boiling point.

the PL mapping across the lateral channel, the treated films exhibited a weaker decay constant and significantly less iodine defect migration than untreated $MAPbI_3$ (Fig. 2, G and H). When $MAPbI_3$ films were dipped in methyl acetate as the Lewis base for 24 hours and monitored by XRD at regular intervals, we also observed a change in lattice constant from 6.18 to 6.22 Å, which could indicate incorporation of the solvent into the crystal lattice or potentially relaxation of strain due to a reduced defect/vacancy (Fig. 4D). No difference in the XRD pattern was obtained when the perovskite layer was treated only for short times in the same way as used for device fabrication (details in Materials and Methods), indicating that for short exposure, the effect is limited to a thin surface layer.

We performed such Lewis base, positive azeotrope treatments also on Rb-passivated $CsFAMAPbI_3$-based perovskite FETs, and this resulted in improvement in the injection-limited behavior in the output characteristics (Fig. 5A) and observation of a clean hysteresis-free output and transfer characteristics with a $\mu_{FET}$ reaching values of 1.2 $cm^2/V\cdot s$ (Fig. 5B). Details of the $\mu_{FET}$ versus $V_g$ are shown in fig. S26A, and the histogram distribution of mobility is depicted in fig. S26B. We further confirmed the operational stability of the perovskite FETs through voltage bias stress measurements. The devices were operated continuously for 10 hours in a transdiode mode ($V_d = V_g = 60$ V), and the shift in threshold voltage ($V_{th}$) was monitored. We observe a pronounced improvement in the threshold voltage shift ($\Delta V_t$) stability. Devices fabricated with pristine $MAPbI_3$ thin films exhibited $\Delta V_t \sim 10$ V after 10 hours of continuous operation while devices fabricated with solvent-treated $RbCsFAMAPbI_3$ exhibit only $\Delta V_t \sim 2$ V after the same stress (Fig. 5C). Subsequently, the transistors recover to their original characteristics upon removal of bias stress. This degree of threshold voltage stability (~3% of the operating voltage) has never been demonstrated for a perovskite FETs and is approaching that of other transistor technologies, such as organic or amorphous silicon transistors.

## Optimization of p-type perovskite FETs

Inspired by these results, we also investigated p-type perovskites and aimed to translate the strategies learned from the n-type perovskite FETs to p-type devices. Demonstration of gate modulation in thin films of p-type perovskite FETs has hitherto been difficult at room temperature. We were able to observe room temperature p-type transfer characteristics in $FA_{0.8}MA_{0.2}PbBr_3$ ($FAMAPbBr_3$) with a mobility $\mu_{FET} \sim 0.005$ $cm^2/V\cdot s$ (section S12). When using cationic compositions comprising Cs with bromide perovskites, however, no gate modulation (fig. S30C) was observed at room temperature. This could be attributed to the stronger propensity to CsBr formation, resulting in a phase-segregated nonperovskite phase in the material (*35*). When $FAMAPbBr_3$ FETs were treated with Lewis base solvents (like diethyl ether or methyl acetate), we observed degradation of the charge transport characteristics (fig. S29). However, when the p-type $FAMAPbBr_3$ layer was treated with the Lewis acid 1,3,5-tribromobenzene instead, we observed an improvement in the transistor performance and a clean hysteresis-free p-type transistor performance with $\mu_{FET} \sim 0.02$ $cm^2/V\cdot s$ (Fig. 5D and fig. S30B). This suggests that in the p-type devices, there is a density of hole traps

Downloaded from http://advances.sciencemag.org/ on April 10, 2020

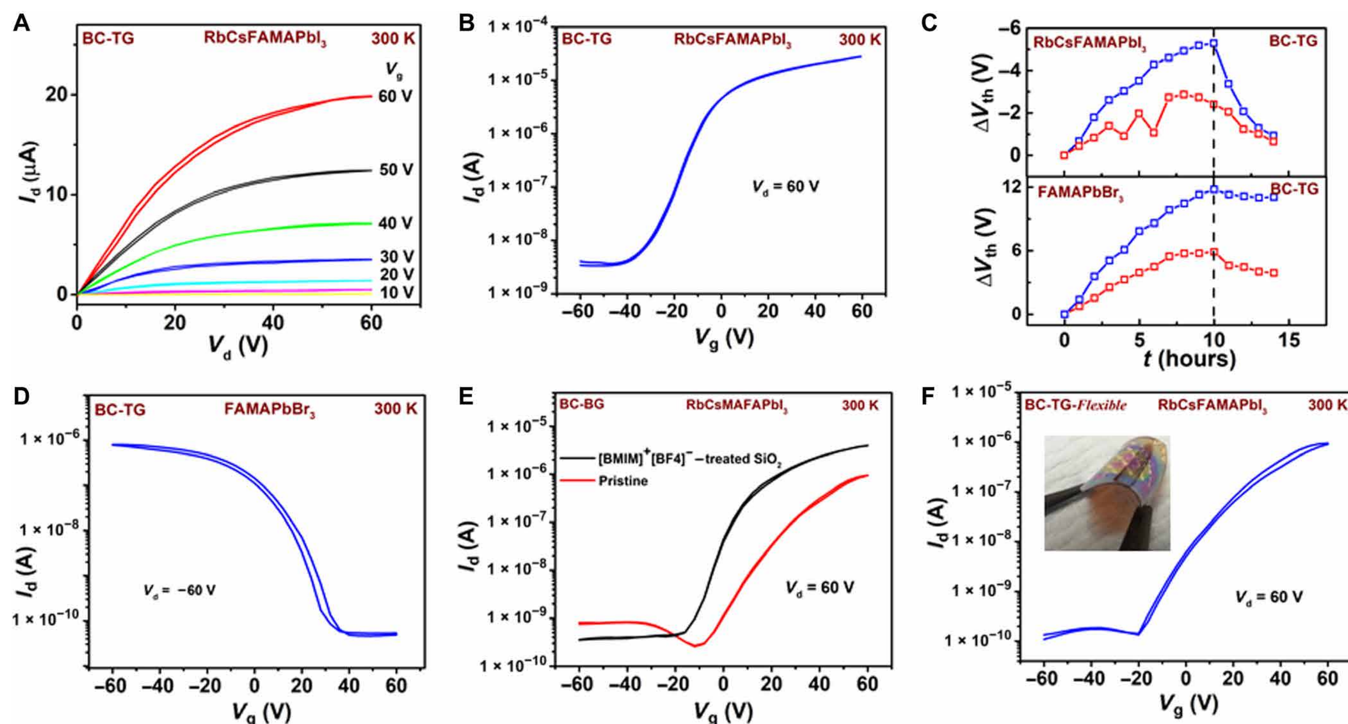


**Fig. 5. Performance of optimized p-type and n-type, top-gate and bottom-gate multiple cation perovskite FETs.** (**A**) Room temperature output and (**B**) transfer characteristics of bottom-contact, top-gate (BC-TG) FETs ($L = 100$ μm, $W = 1$ mm) fabricated from diethyl ether–treated $RbCsFAMAPbI_3$. (**C**) Comparison of voltage stress stability measured on bottom-contact, top-gate (BC-TG) FETs fabricated from pristine (blue) and diethyl ether–treated (red) perovskite layers of $RbCsFAMAPbI_3$ (top) and pristine (blue) as well as 1,3,5-tribromobenzene–treated (blue) perovskite layer of $FAMAPbBr_3$ (bottom). (**D**) Transfer characteristics depicting optimized p-type bottom-contact, top-gate perovskite transistor (BC-TG) FETs ($L = 100$ μm, $W = 1$ mm) fabricated from 1,3,5-tribromobenzene solvent–treated $FAMAPbBr_3$ perovskite layer. (**E**) Room temperature transfer characteristics measured on bottom-contact, bottom-gate (BC-BG) $RbCsFAMAPbI_3$-based perovskite FETs ($L = 100$ μm, $W = 1$ mm) fabricated on ionic liquid $[BMIM]^+$ $[BF_4]^-$–treated $SiO_2$ interface (black) and pristine $SiO_2$ interface (red). (**F**) Bottom-contact, top-gate (BC-TG) flexible perovskite FETs ($L = 100$ μm, $W = 1$ mm) fabricated with diethyl ether–treated $RbCsFAMAPbI_3$. Photo credit: Satyaprasad P. Senanayak, University of Cambridge, UK.

caused by structural defects and vacancies in the perovskite or by impurities such as water that can be eliminated/passivated by an electron-withdrawing Lewis acid treatment.

### Optimization of bottom-gated perovskite structure

We also explored the optimization of device performance through acid/base treatments in bottom-gate device architectures. However, the solvent-based Lewis acid or base treatments discussed above, which worked well for bottom-contact, top-gate perovskite FETs, did not have any effect on the performance of bottom-contact, bottom-gate devices on $Si/SiO_2$ wafers due to the fact that the effect of solvent effect is mainly limited to the surface and does not affect the buried interface between the perovskite and the $SiO_2$ gate dielectric (fig. S31). We explored instead the effect of halides such as $F^-$ and $I^-$ and divalent additives like $Zn^{2+}$ and $Cd^{2+}$ that behave as soft Lewis bases and acids. We introduced $F^-$ ions at the interface by spin coating 1-butyl-3-methylimidazolium tetrafluoroborate–based ionic liquid (IL). $I^-$ ions were introduced through $NH_3$-terminated self-assembled monolayers (SAMs) (3-aminopropyl)triethoxysilane (APTES) that were treated with HI to obtain iodide termination (details in Materials and Methods). $RbCsFAMAPbI_3$ devices fabricated on IL- or SAM-treated interfaces exhibited enhanced performance (Fig. 5E and fig. S32) and $\mu_{FET}$ increased from ~0.1 to up to 0.3 $cm^2/V{\cdot}s$. However, addition of divalent cations like $ZnI_2$ (details in Materials and Methods), which are Lewis acids, into n-type $RbCsFAMAPbI_3$ led to a decrease in the ON current and a minor increase in the OFF current with an overall $\mu_{FET}$ of $10^{-3}$ $cm^2/V{\cdot}s$ (fig. S33). On the other hand, when divalent cationic salts like $ZnBr_2$ or $ZnI_2$ (in varying composition) were added into p-type $FAMAPbBr_3$ and $FA_{0.85}MA_{0.15}(Pb_{0.5}Sn_{0.5})I_3$ [referred to as $FAMA(PbSn)I_3$ hereafter], respectively, we observed significant enhancement in the channel current by an order of magnitude and $\mu_{FET}$ increased from 0.002 to 0.007 $cm^2/V{\cdot}s$, with the best $\mu_{FET}$ observed for samples passivated with 5% $ZnI_2$ (figs. S34 to S35). The bias stress instability in the bottom-gated $RbCsFAMAPbI_3$ devices also decreased from $\Delta V_{th} \sim -17$ to $\sim -5$ V upon introduction of Lewis base $I^-$ at the interface (fig. S36). We also evaluated mixed Pb-Sn bottom-gate perovskite FETs based on $FAMA(PbSn)I_3$ that also exhibited p-type characteristics and showed improved bias stress stability from $\Delta V_{th} \sim 14$ to $\sim 9$ V upon passivation with Lewis acid–based ZnI salts (fig. S36).

Last, to demonstrate that stable perovskite films can be obtained by low-temperature processing, we fabricated bottom-contact, top-gate perovskite transistors on poly(ethylene terephthalate) (PET) substrates. $RbCsFAMAPbI_3$ devices on PET exhibited hysteresis-free characteristics similar to those on glass substrates, but with a marginal drop in the $\mu_{FET} \sim 0.5$ $cm^2/V{\cdot}s$. This may be due to the difference in the surface energy or roughness between glass and PET substrates (Fig. 5F).



Downloaded from http://advances.sciencemag.org/ on April 10, 2020

## DISCUSSION

Detailed investigation of FET performance among different compositions of perovskite materials fabricated from different composition indicates the low tolerance of perovskite materials to small variations in precursor stoichiometry. Despite major differences in the operation of photovoltaics and FETs, it is interesting to observe that only certain compositions exhibit excellent performance. Moreover, a small variation of about 0.05% variation from the high-performing composition is enough to significantly affect the overall performance as well as the stability of optoelectronic devices (*60*). This can be related to the formation of phase-pure perovskite, stable lattice structure with a low degree of disorder.

## CONCLUSION

Our work demonstrates a practical strategy for obtaining operationally stable, hysteresis-free perovskite transistors with performance approaching the level required for large area integrated electronic applications. By incorporating appropriate small inorganic cations, such as Cs, into the perovskite lattice and using passivation agents, such as Rb, we have been able to reduce ionic defect migration at room temperature to a level at which it does no longer manifest itself in device hysteresis. Furthermore, with solvent treatments based on Lewis base and Lewis acid azeotropes, we achieve further optimization in device performance and stability for n-type and p-type operation, respectively. Our work opens up the possibility of using these materials for application prospects in large area electronics, for example, as n-type devices in complementary circuits with high-mobility p-type organic semiconductors, and makes FET architectures a more powerful tool for investigating the charge transport physics of perovskite semiconductors. Moreover, the understanding of the instability and strategies evolved would inspire analogous techniques for improving the efficiency and stability of perovskite LEDs and solar cells.

## MATERIALS AND METHODS

### Perovskite film preparation

$CH_3NH_3I$ was synthesized according to a previously reported procedure (*25*). Absolute ethanol (100 ml) was used to dilute 24 ml of methylamine solution (33% in ethanol) in a 250-ml round bottom flask, followed by the addition of 10 ml of aqueous solution of hydriodic acid [57 weight % (wt %)] under constant stirring. After 1 hour of reaction time at room temperature, a rotary evaporator was used to remove the solvents from the reaction mixture. The white solid residual was then washed using dry diethyl ether and recrystallized from ethanol to obtain MA iodide crystals ($CH_3NH_3I$). Other precursor materials, which include lead(II) acetate trihydrate, cesium iodide, rubidium iodide, cesium bromide, rubidium bromide, and tin iodide, were used as obtained from Sigma-Aldrich. Similarly, precursor materials FA iodide, FA bromide, and MA bromide were obtained from GreatCell Solar Inc. and used as received. The precursor solutions for the perovskite material were obtained by mixing the respective precursor materials in *N*,*N*′-dimethylformamide (DMF) at 0.75 M concentration to obtain $MAPbI_3$, $FA_{0.2}MA_{0.8}PbI_3$, $FA_{0.05}MA_{0.95}PbI_3$, $FA_{0.1}MA_{0.9}PbI_3$, and $FA_{0.8}MA_{0.2}PbBr_3$ and in DMF:dimethyl sulfoxide (4:1) at 0.75 M concentration for $Cs_{0.05}FA_{0.17}MA_{0.78}PbI_3$, $Rb_{0.05}Cs_{0.05}FA_{0.15}MA_{0.75}PbI_3$, $Cs_{0.05}FA_{0.17}MA_{0.78}PbBr_3$, and $FA_{0.85}MA_{0.15}(Pb_{0.5}Sn_{0.5})I_3$. Freshly prepared precursor solutions were spin-coated using the antisolvent technique at 5000 rpm for 3 min and annealed at 100°C for 30 min. The above compositions reflect the concentration of the different cations/anions in solution. This is not meant to suggest that they are necessarily incorporated into the solid perovskite lattice in the same proportions; it is known, for example, that Rb is not incorporated into the perovskite lattice but merely acts to modify the crystallization kinetics and potentially passivates defects at grain boundaries.

### FET fabrication and measurement

Bottom-contact, top-gate FETs were fabricated on Cr/Au (3 nm:22 nm) source-drain electrodes that were evaporated and patterned photolithographically on precleaned, plasma-treated glass substrates. This was followed by the deposition of the perovskite layer as described above. For the solvent treatment of the perovskite layer, an orthogonal solvent is introduced on top of the perovskite layer for 2 min, covering the surface of the perovskite film. This was followed by spinning the solvents off the perovskite film at 2000 rpm for 60 s and annealing the solvent-treated perovskite films at 100°C for 30 min. A Cytop dielectric layer of ~500-nm thickness was then spin-coated over the perovskite film and annealed at 90°C for 20 min. The devices were then completed by evaporating the Au gate electrode (25 nm) through a shadow mask. For flexible devices, this method was adopted on PET substrates. For bottom-contact, bottom-gate devices, lithographically patterned source-drain electrodes were obtained on $n^{++}$-type Si (100) wafers (resistivity, <0.005 ohm·cm; Active Business Company GmbH) with 300 nm of $SiO_2$ layer (capacitance, $C_i = 11.5$ nF cm$^{-2}$). All the transfer characteristics were measured in pulsed mode, and the output characteristics were measured in continuous mode using an Agilent 4155B parameter analyzer. Note that in the pulsed mode of operation, for the transfer measurement, $V_g$ was applied over a short impulse of 0.5 ms. In the continuous mode of operation, the voltages were applied continuously during the scan. To ensure reproducibility of the device and avoid any degradation of the interface, all the steps for device fabrication were performed in a nitrogen-filled glove box.

### SAM treatment

APTES was purchased from Sigma-Aldrich and used as received (storage under a $N_2$ atmosphere). Si/$SiO_2$ wafers were fully immersed for 45 min in a 4 mM APTES solution in anhydrous toluene. Following the treatment, wafers were rinsed by toluene, acetone, and isopropanol and then sonicated for 5 min in fresh toluene. $NH_2$-SAM is converted to $NH_3I$-SAM by treating the wafers in a 1 mM solution of HI in water for 1 min and then annealing at 100°C for 10 min. Devices were then fabricated on these SAM-treated Si/$SiO_2$ substrates.

### Ionic layer

1-Butyl-3-methylimidazolium tetrafluoroborate (0.1 wt %) was dissolved in methanol solution and spin-coated at 2000 rpm for 60 s followed by annealing at 100°C for 30 min.

### $ZnI_2$ and $CdI_2$

For introducing group 12 salts, $ZnI_2$ and $CdI_2$ were mixed with FAI in 1:1 mixture and then added with varied composition into the respective perovskite mixture.

### Bias stress measurements

Considering the fact that defect migration due to high operating voltage is a primary cause of operational instability in perovskite transistors, voltage bias stress measurements were performed while

Downloaded from http://advances.sciencemag.org/ on April 10, 2020

the transistor was operated continuously in a transdiode mode at $V_d = V_g = 60$ V. Transfer curves were measured every 1 hour, and the shift in the threshold voltage was extracted as a measure of operational stability.

### THz absorption spectroscopy

Broadband THz time-domain spectroscopy was carried out with a Tera K15-T-Light MENLO system on back-gated, bottom-contact perovskite transistors. The measurement involved pulses from a 30-mW pump laser of 90 fs duration at 1560 nm (repetition rate of 100 MHz) that is split into two paths: (i) a component focused down to a 40-μm spot onto the THz emitter, resulting in a broadband THz emission with a spot size of ~1 mm, and (ii) a component through the delay stage for coherent THz detection. For the back-gated transistor, mildly doped Si/$SiO_2$ (~10 ohm·cm) substrates were used on which lithographically patterned Au source and drain electrodes were fabricated ($L = 80$ μm, $W = 2.3$ cm). This was followed by coating the perovskite layer in the same way as described above. The devices were then completed by coating a layer of Cytop to prevent any unwanted exposure of the perovskite samples to ambient condition. To avoid any degradation of the perovskite films and eliminate the features from water absorption, the measurements were performed in a nitrogen environment with a humidity level of <5%. Absorption spectra are obtained from fast Fourier transforms of the time-resolved response (averaged over 4000 waveforms) from the perovskite film, and the spectra were normalized to the response of a device without the perovskite layer.

### Porosity analysis of the perovskite films

To obtain the porosity of the perovskite films, $N_2$ adsorption isotherms were measured on perovskite thin films fabricated on glass substrates (used for FET fabrication) at 77 K using a Micromeritics 3Flex instrument. Before the adsorption measurement, all samples were degassed at 100°C for 1 hour under high vacuum ($10^{-6}$ mbar) to ensure that the pores of the perovskite films are as free as possible from any adsorbates or residual solvent without sample degradation. The isotherms were then measured without exposing them to ambient condition.

### ESR measurement

All electron spin resonance (ESR) spectra were taken in an Oxford Instruments ESR900 cryostat with a Bruker E500 X-band spectrometer. Measurements were recorded at a microwave frequency of approximately 9.4 GHz and a microwave power of 20 mW. The external field was modulated at a modulation frequency of $\omega_{mod} = 100$ kHz to allow lock-in measurements and the modulation amplitude was $B_{mod} = 1$ G. These values were chosen such that the material was not saturated; i.e., the spins had enough time to relax between modulation cycles. [Equivalently, $\omega_{mod}B_{mod} << (\gamma T_1 T_2)^{-1}$, where $T_1$ and $T_2$ are the longitudinal and transverse spin relaxation times, respectively.] The number of spins is found by integration of the absorption spectrum (i.e., double integration of the ESR signal) using the following expression: $N_{spins} = \frac{k \times \text{Area} \times k_B T}{B_{mw} B_0 S(S+1) \hbar\omega_{mw}}$, where $k$ is a calibration factor for the spectrometer and sample position, $B_0$ is the Zeeman field, $S$ is the spin (=1/2 for electrons), $\omega_{mw}$ is the microwave frequency, $k_B$ is the Boltzmann constant, and $B_{mw}$ is the microwave field measured from the microwave power using the following expression: (calibration constant) × $(Q \times P_{mw})^{1/2}$, where $Q$ is the quality factor of the cavity and $P_{mw}$ is the microwave power.

### PL mapping

PL measurements were performed using a confocal microscope (WITec, Alpha RAS system). A fiber-coupled 405-nm continuous-wave laser (Coherent, CUBE) was focused onto the sample using 40× objective. The average power of the laser at its focal point was 0.5 μW. The PL of the sample was collected in the reflection geometry from the same objective while the excitation laser beam from the reflection is blocked using a 415-nm long-pass filter. The sample was mounted on an XYZ translation stage (piezo-electric) and raster-scanned in 1-μm steps to collect the PL locally. Au-coated tungsten tips (having magnetic base) were used to contact the source and drain electrodes. The source-drain bias is applied using a Keithley 2400 source meter. The collected PL spectrum was measured using a calibrated Si–charge-coupled device array detector (Andor, iDus BR-DD) fitted to a monochromator. All movements of the stage were automated and controlled by WITec ScanCtr spectroscopy Plus software. All PL spectra were performed in a $N_2$ atmosphere and averaged 10 times during the acquisition process. The measurements were repeated on three devices for consistency.

## SUPPLEMENTARY MATERIALS

Supplementary material for this article is available at http://advances.sciencemag.org/cgi/content/full/6/15/eaaz4948/DC1

## REFERENCES AND NOTES


1. P. K. Nayak, S. Mahesh, H. J. Snaith, D. Cahen, Photovoltaic solar cell technologies: Analysing the state of the art. *Nat. Rev. Mater.* **4**, 269–285 (2019).
2. B. Zhao, S. Bai, V. Kim, R. Lamboll, R. Shivanna, F. Auras, J. M. Richter, L. Yang, L. Dai, M. Alsari, X.-J. She, L. Liang, J. Zhang, S. Lilliu, P. Gao, H. J. Snaith, J. Wang, N. C. Greenham, R. H. Friend, D. Di, High-efficiency perovskite–polymer bulk heterostructure light-emitting diodes. *Nat. Photonics* **12**, 783–789 (2018).
3. S. D. Stranks, H. J. Snaith, Metal-halide perovskites for photovoltaic and light-emitting devices. *Nat. Nanotechnol.* **10**, 391–402 (2015).
4. S. D. Stranks, G. E. Eperon, G. Grancini, C. Menelaou, M. J. P. Alcocer, T. Leijtens, L. M. Herz, A. Petrozza, H. J. Snaith, Electron-hole diffusion lengths exceeding 1 micrometer in an organometal trihalide perovskite absorber. *Science* **342**, 341–344 (2013).
5. A. Miyata, A. Mitioglu, P. Plochocka, O. Portugall, J. T.-W. Wang, S. D. Stranks, H. J. Snaith, R. J. Nicholas, Direct measurement of the exciton binding energy and effective masses for charge carriers in organic–inorganic tri-halide perovskites. *Nat. Phys.* **11**, 582–587 (2015).
6. T. Wang, B. Daiber, J. M. Frost, S. A. Mann, E. C. Garnett, A. Walsh, B. Ehrler, Indirect to direct bandgap transition in methylammonium lead halide perovskite. *Energ. Environ. Sci.* **10**, 509–515 (2017).
7. J. A. Christians, P. Schulz, J. S. Tinkham, T. H. Schloemer, S. P. Harvey, B. J. Tremolet de Villers, A. Sellinger, J. J. Berry, J. M. Luther, Tailored interfaces of unencapsulated perovskite solar cells for >1,000 hour operational stability. *Nat. Energy* **3**, 68–74 (2018).
8. Y. Hou, X. Du, S. Scheiner, D. P. McMeekin, Z. Wang, N. Li, M. S. Killian, H. Chen, M. Richter, I. Levchuk, N. Schrenker, E. Spiecker, T. Stubhan, N. A. Luechinger, A. Hirsch, P. Schmuki, H.-P. Steinrück, R. H. Fink, M. Halik, H. J. Snaith, C. J. Brabec, A generic interface to reduce the efficiency-stability-cost gap of perovskite solar cells. *Science* **358**, 1192–1197 (2017).
9. H. Zhu, A. Liu, H. L. Luque, H. Sun, D. Ji, Y.-Y. Noh, Perovskite and conjugated polymer wrapped semiconducting carbon nanotube hybrid films for high-performance transistors and phototransistors. *ACS Nano* **13**, 3971–3981 (2019).
10. A. N. Aleshin, I. P. Shcherbakov, E. V. Gushchina, L. B. Matyushkin, V. A. Moshnikov, Solution-processed field-effect transistors based on polyfluorene–cesium lead halide nanocrystals composite films with small hysteresis of output and transfer characteristics. *Org. Electron.* **50**, 213–219 (2017).
11. L. Zhu, H. Zhang, Q. Lu, Y. Wang, Z. Deng, Y. Hu, Z. Lou, Q. Cui, Y. Hou, F. Teng, Synthesis of ultrathin two-dimensional organic–inorganic hybrid perovskite nanosheets for polymer field-effect transistors. *J. Mater. Chem. C* **6**, 3945–3950 (2018).
12. N. Arora, M. I. Dar, A. Hinderhofer, N. Pellet, F. Schreiber, S. M. Zakeeruddin, M. Grätzel, Perovskite solar cells with CuSCN hole extraction layers yield stabilized efficiencies greater than 20%. *Science* **358**, 768–771 (2017).
13. J. You, L. Meng, T.-B. Song, T.-F. Guo, Y. Yang, W.-H. Chang, Z. Hong, H. Chen, H. Zhou, Q. Chen, Y. Liu, N. De Marco, Y. Yang, Improved air stability of perovskite solar cells via solution-processed metal oxide transport layers. *Nat. Nanotechnol.* **11**, 75–81 (2016).


Downloaded from http://advances.sciencemag.org/ on April 10, 2020

14. M. Saliba, T. Matsui, K. Domanski, J.-Y. Seo, A. Ummadisingu, S. M. Zakeeruddin, J.-P. Correa-Baena, W. R. Tress, A. Abate, A. Hagfeldt, M. Grätzel, Incorporation of rubidium cations into perovskite solar cells improves photovoltaic performance. *Science*, 206–209 (2016).
15. Z. Wang, Q. Lin, F. P. Chmiel, N. Sakai, L. M. Herz, H. J. Snaith, Efficient ambient-air-stable solar cells with 2D–3D heterostructured butylammonium-caesium-formamidinium lead halide perovskites. *Nat. Energy* **2**, 17135 (2017).
16. H. Tsai, W. Nie, J.-C. Blancon, C. C. Stoumpos, R. Asadpour, B. Harutyunyan, A. J. Neukirch, R. Verduzco, J. J. Crochet, S. Tretiak, L. Pedesseau, J. Even, M. A. Alam, G. Gupta, J. Lou, P. M. Ajayan, M. J. Bedzyk, M. G. Kanatzidis, A. D. Mohite, High-efficiency two-dimensional Ruddlesden–Popper perovskite solar cells. *Nature* **536**, 312–316 (2016).
17. K. Lin, J. Xing, L. N. Quan, F. P. G. de Arquer, X. Gong, J. Lu, L. Xie, W. Zhao, D. Zhang, C. Yan, W. Li, X. Liu, Y. Lu, J. Kirman, E. H. Sargent, Q. Xiong, Z. Wei, Perovskite light-emitting diodes with external quantum efficiency exceeding 20 per cent. *Nature* **562**, 245–248 (2018).
18. Y. Jia, R. A. Kerner, A. J. Grede, B. P. Rand, N. C. Giebink, Continuous-wave lasing in an organic–inorganic lead halide perovskite semiconductor. *Nat. Photonics* **11**, 784–788 (2017).
19. X. Y. Chin, D. Cortecchia, J. Yin, A. Bruno, C. Soci, Lead iodide perovskite light-emitting field-effect transistor. *Nat. Commun.* **6**, 7383 (2015).
20. F. Li, C. Ma, H. Wang, W. Hu, W. Yu, A. D. Sheikh, T. Wu, Ambipolar solution-processed hybrid perovskite phototransistors. *Nat. Commun.* **6**, 8238 (2015).
21. Y. Mei, C. Zhang, Z. V. Vardeny, O. D. Jurchescu, Electrostatic gating of hybrid halide perovskite field-effect transistors: Balanced ambipolar transport at room-temperature. *MRS Commun.* **5**, 297–301 (2015).
22. D. Li, G. Wang, H.-C. Cheng, C.-Y. Chen, H. Wu, Y. Liu, Y. Huang, X. Duan, Size-dependent phase transition in methylammonium lead iodide perovskite microplate crystals. *Nat. Commun.* **7**, 11330 (2016).
23. J. G. Labram, D. H. Fabini, E. E. Perry, A. J. Lehner, H. Wang, A. M. Glaudell, G. Wu, H. Evans, D. Buck, R. Cotta, L. Echegoyen, F. Wudl, R. Seshadri, M. L. Chabinyc, Temperature-dependent polarization in field-effect transport and photovoltaic measurements of methylammonium lead iodide. *J. Phys. Chem. Lett.* **6**, 3565–3571 (2015).
24. W. Yu, F. Li, L. Yu, M. R. Niazi, Y. Zou, D. Corzo, A. Basu, C. Ma, S. Dey, M. L. Tietze, U. Buttner, X. Wang, Z. Wang, M. N. Hedhili, C. Guo, T. Wu, A. Amassian, Single crystal hybrid perovskite field-effect transistors. *Nat. Commun.* **9**, 5354 (2018).
25. S. P. Senanayak, B. Yang, T. H. Thomas, N. Giesbrecht, W. Huang, E. Gann, B. Nair, K. Goedel, S. Guha, X. Moya, C. R. McNeill, P. Docampo, A. Sadhanala, R. H. Friend, H. Sirringhaus, Understanding charge transport in lead iodide perovskite thin-film field-effect transistors. *Sci. Adv.* **3**, e1601935 (2017).
26. Y.-H. Lin, P. Pattanasattayavong, T. D. Anthopoulos, Metal-halide perovskite transistors for printed electronics: Challenges and opportunities. *Adv. Mater.* **29**, 1702838 (2017).
27. M. Saliba, T. Matsui, J.-Y. Seo, K. Domanski, J.-P. Correa-Baena, M. K. Nazeeruddin, S. M. Zakeeruddin, W. Tress, A. Abate, A. Hagfeldt, M. Grätzel, Cesium-containing triple cation perovskite solar cells: Improved stability, reproducibility and high efficiency. *Energ. Environ. Sci.* **9**, 1989–1997 (2016).
28. A. R. B. M. Yusoff, H. P. Kim, X. Li, J. Kim, J. Jang, M. K. Nazeeruddin, Ambipolar triple cation perovskite field effect transistors and inverters. *Adv. Mater.* **29**, 1602940 (2017).
29. P. F. Ndione, Z. Li, K. Zhu, Effects of alloying on the optical properties of organic–inorganic lead halide perovskite thin films. *J. Mater. Chem. C* **4**, 7775–7782 (2016).
30. L. M. Herz, Charge-carrier mobilities in metal halide perovskites: Fundamental mechanisms and limits. *ACS Energy Lett.* **2**, 1539–1548 (2017).
31. N. Onoda-Yamamuro, T. Matsuo, H. Suga, Dielectric study of $CH_3NH_3PbX_3$ (X = Cl, Br, I). *J. Phys. Chem. Solid* **53**, 935–939 (1992).
32. J. M. Frost, K. T. Butler, F. Brivio, C. H. Hendon, M. van Schilfgaarde, A. Walsh, Atomistic origins of high-performance in hybrid halide perovskite solar cells. *Nano Lett.* **14**, 2584–2590 (2014).
33. F. Ma, J. Li, W. Li, N. Lin, L. Wang, J. Qiao, Stable $\alpha/\delta$ phase junction of formamidinium lead iodide perovskites for enhanced near-infrared emission. *Chem. Sci.* **8**, 800–805 (2017).
34. A. Binek, F. C. Hanusch, P. Docampo, T. Bein, Stabilization of the trigonal high-temperature phase of formamidinium lead iodide. *J. Phys. Chem. Lett.* **6**, 1249–1253 (2015).
35. Y. Hu, M. F. Aygüler, M. L. Petrus, T. Bein, P. Docampo, Impact of rubidium and cesium cations on the moisture stability of multiple-cation mixed-halide perovskites. *ACS Energy Lett.* **2**, 2212–2218 (2017).
36. Y. Hu, E. M. Hutter, P. Rieder, I. Grill, J. Hanisch, M. F. Aygüler, A. G. Hufnagel, M. Handloser, T. Bein, A. Hartschuh, K. Tvingstedt, V. Dyakonov, A. Baumann, T. J. Savenije, M. L. Petrus, P. Docampo, Understanding the role of cesium and rubidium additives in perovskite solar cells: Trap states, charge transport, and recombination. *Adv. Energy Mater.* **8**, 1703057 (2018).
37. M. Abdi-Jalebi, Z. Andaji-Garmaroudi, S. Cacovich, C. Stavrakas, B. Philippe, J. M. Richter, M. Alsari, E. P. Booker, E. M. Hutter, A. J. Pearson, S. Lilliu, T. J. Savenije, H. Rensmo, G. Divitini, C. Ducati, R. H. Friend, S. D. Stranks, Maximizing and stabilizing luminescence from halide perovskites with potassium passivation. *Nature* **555**, 497–501 (2018).
38. C. Besleaga, L. E. Abramiuc, V. Stancu, A. G. Tomulescu, M. Sima, L. Trinca, N. Plugaru, L. Pintilie, G. A. Nemnes, M. Iliescu, H. G. Svavarsson, A. Manolescu, I. Pintilie, Iodine migration and degradation of perovskite solar cells enhanced by metallic electrodes. *J. Phys. Chem. Lett.* **7**, 5168–5175 (2016).
39. C. Li, A. Guerrero, Y. Zhong, A. Gräser, C. A. M. Luna, J. Köhler, J. Bisquert, R. Hildner, S. Huettner, Real-time observation of iodide ion migration in methylammonium lead halide perovskites. *Small* **13**, 1701711 (2017).
40. A. Senocrate, I. Moudrakovski, G. Y. Kim, T.-Y. Yang, G. Gregori, M. Grätzel, J. Maier, The nature of ion conduction in methylammonium lead iodide: A multimethod approach. *Angew. Chem. Int. Ed.* **56**, 7755–7759 (2017).
41. D. W. de Quilettes, W. Zhang, V. M. Burlakov, D. J. Graham, T. Leijtens, A. Osherov, V. Bulović, H. J. Snaith, D. S. Ginger, S. D. Stranks, Photo-induced halide redistribution in organic–inorganic perovskite films. *Nat. Commun.* **7**, 11683 (2016).
42. W. Bollmann, N. F. Uvarov, E. F. Hairetdinov, Estimation of point defect parameters of solids on the basis of a defect formation model of melting (II). Vacancy formation enthalpy in relation to the heat of fusion and the increase of volume due to melting. *Cryst. Res. Technol.* **24**, 421–435 (1989).
43. I. A. Shkrob, T. W. Marin, Charge trapping in photovoltaically active perovskites and related halogenoplumbate compounds. *J. Phys. Chem. Lett.* **5**, 1066–1071 (2014).
44. S. Colella, M. Todaro, S. Masi, A. Listorti, D. Altamura, R. Caliandro, C. Giannini, E. Carignani, M. Geppi, D. Meggiolaro, G. Buscarino, F. De Angelis, A. Rizzo, Light-induced formation of $Pb^{3+}$ paramagnetic species in lead halide perovskites. *ACS Energy Lett.* **3**, 1840–1847 (2018).
45. Q. Sun, X. Liu, J. Cao, R. I. Stantchev, Y. Zhou, X. Chen, E. P. J. Parrott, J. Lloyd-Hughes, N. Zhao, E. Pickwell-MacPherson, Highly sensitive terahertz thin-film total internal reflection spectroscopy reveals in situ photoinduced structural changes in methylammonium lead halide perovskites. *J. Phys. Chem. C* **122**, 17552–17558 (2018).
46. A. M. A. Leguy, A. R. Goñi, J. M. Frost, J. Skelton, F. Brivio, X. Rodríguez-Martínez, O. J. Weber, A. Pallipurath, M. I. Alonso, M. Campoy-Quiles, M. T. Weller, J. Nelson, A. Walsh, P. R. F. Barnes, Dynamic disorder, phonon lifetimes, and the assignment of modes to the vibrational spectra of methylammonium lead halide perovskites. *Phys. Chem. Chem. Phys.* **18**, 27051–27066 (2016).
47. U. Aschauer, R. Pfenninger, S. M. Selbach, T. Grande, N. A. Spaldin, Strain-controlled oxygen vacancy formation and ordering in $CaMnO_3$. *Phys. Rev. B* **88**, 054111 (2013).
48. M. I. Saidaminov, J. Kim, A. Jain, R. Quintero-Bermudez, H. Tan, G. Long, F. Tan, A. Johnston, Y. Zhao, O. Voznyy, E. H. Sargent, Suppression of atomic vacancies via incorporation of isovalent small ions to increase the stability of halide perovskite solar cells in ambient air. *Nat. Energy* **3**, 648–654 (2018).
49. P. A. Bobbert, A. Sharma, S. G. J. Mathijssen, M. Kemerink, D. M. de Leeuw, Operational stability of organic field-effect transistors. *Adv. Mater.* **24**, 1146–1158 (2012).
50. N. Aristidou, C. Eames, I. Sanchez-Molina, X. Bu, J. Kosco, M. S. Islam, S. A. Haque, Fast oxygen diffusion and iodide defects mediate oxygen-induced degradation of perovskite solar cells. *Nat. Commun.* **8**, 15218 (2017).
51. M. Nikolka, I. Nasrallah, B. Rose, M. K. Ravva, K. Broch, A. Sadhanala, D. Harkin, J. Charmet, M. Hurhangee, A. Brown, S. Illig, P. Too, J. Jongman, I. M. Culloch, J.-L. Bredas, H. Sirringhaus, High operational and environmental stability of high-mobility conjugated polymer field-effect transistors through the use of molecular additives. *Nat. Mater.* **16**, 356–362 (2016).
52. A. Ciccioli, A. Latini, Thermodynamics and the intrinsic stability of lead halide perovskites $CH_3NH_3PbX_3$. *J. Phys. Chem. Lett.* **9**, 3756–3765 (2018).
53. J. Huang, S. Tan, P. D. Lund, H. Zhou, Impact of $H_2O$ on organic–inorganic hybrid perovskite solar cells. *Energ. Environ. Sci.* **10**, 2284–2311 (2017).
54. T. Baikie, Y. Fang, J. M. Kadro, M. Schreyer, F. Wei, S. G. Mhaisalkar, M. Graetzel, T. J. White, Synthesis and crystal chemistry of the hybrid perovskite $(CH_3NH_3)PbI_3$ for solid-state sensitised solar cell applications. *J. Mater. Chem. A* **1**, 5628–5641 (2013).
55. M. Nikolka, G. Schweicher, J. Armitage, I. Nasrallah, C. Jellett, Z. Guo, M. Hurhangee, A. Sadhanala, I. McCulloch, C. B. Nielsen, H. Sirringhaus, Performance improvements in conjugated polymer devices by removal of water-induced traps. *Adv. Mater.* **30**, 1801874 (2018).
56. D. W. G. Oxtoby, H. P. Gillis, L. J. Butler, *Principles of Modern Chemistry* (Brooks Cole., ed. 4, 2015).
57. L. H. Horsley, *Azeotropic Data—III* (American Chemical Society, 1973), vol. 116.
58. D. Shi, V. Adinolfi, R. Comin, M. Yuan, E. Alarousu, A. Buin, Y. Chen, S. Hoogland, A. Rothenberger, K. Katsiev, Y. Losovyj, X. Zhang, P. A. Dowben, O. F. Mohammed, E. H. Sargent, O. M. Bakr, Low trap-state density and long carrier diffusion in organolead trihalide perovskite single crystals. *Science* **347**, 519–522 (2015).
59. M. Abdi-Jalebi, M. I. Dar, A. Sadhanala, S. P. Senanayak, M. Franckevičius, N. Arora, Y. Hu, M. K. Nazeeruddin, S. M. Zakeeruddin, M. Grätzel, R. H. Friend, Impact of monovalent cation halide additives on the structural and optoelectronic properties of $CH_3NH_3PbI_3$ perovskite. *Adv. Energy Mater.* **6**, 1502472 (2016).
60. P. Fassl, V. Lami, A. Bausch, Z. Wang, M. T. Klug, H. J. Snaith, Y. Vaynzof, Fractional deviations in precursor stoichiometry dictate the properties, performance and stability of perovskite photovoltaic devices. *Energy Environ. Sci.* **11**, 3380–3391 (2018).


Downloaded from http://advances.sciencemag.org/ on April 10, 2020

**Acknowledgments:** S.P.S. acknowledges C. Liu for useful discussion in SQUID measurements. **Funding:** S.P.S. and R.S. acknowledges funding from the Royal Society London for the Newton Fellowship. S.P.S. acknowledges funding through Royal Society Newton Alumni Fellowship. We acknowledge funding from the EPSRC through program grants EP/M005143/1 and EP/P021859/1, as well as other grants EP/P03148X/1, EP/S031103/1, EP/P032591/1. M.A.- J. thanks Cambridge Materials Limited and Wolfson College, University of Cambridge for funding and technical support. G.S. acknowledges postdoctoral fellowship support from The Leverhulme Trust (Early Career Fellowship supported by the Isaac Newton Trust). The authors are grateful for funding from ERC Synergy Grand SC2 (no. 610115). D.F.-J. thanks the Royal Society for funding through a University Research Fellowship. **Author contributions:** S.P.S. performed the experiments on FET, fabricated the devices and samples for different experiments, and wrote the manuscript with inputs from H.S. on the manuscript, data analysis, and design. M.A.-J. assisted S.P.S. in the preparation of mixed perovskite samples and also performed the PDS measurements. R.C. performed the EPR measurements. V.S.K. and H.E.B. performed the THz measurements and D.A.R. provided inputs on the measurement. R.S. and S.P.S. performed the PL mapping measurements. T.T. and D.F.-J. contributed in the $N_2$ adsorption isotherm measurements. N.G. and P.D. synthesized the methylammonium iodide precursor. D.D.N. and S.P.S. performed SQUID measurements. J.W. assisted S.P.S. in the initial measurements of perovskite samples. G.S. grew the SAM layers on the $Si/SiO_2$ substrates. R.H.F. and H.S. supervised the work. All authors discussed the results and revised the manuscript. **Competing interests:** The authors declare that they have no competing interests. **Data and materials availability:** All data needed to evaluate the conclusions in the paper are present in the paper and/or the Supplementary Materials. Additional data related to this paper may be requested from the authors.

Submitted 14 September 2019
Accepted 13 January 2020
Published 10 April 2020
10.1126/sciadv.aaz4948

**Citation:** S. P. Senanayak, M. Abdi-Jalebi, V. S. Kamboj, R. Carey, R. Shivanna, T. Tian, G. Schweicher, J. Wang, N. Giesbrecht, D. Di Nuzzo, H. E. Beere, P. Docampo, D. A. Ritchie, D. Fairen-Jimenez, R. H. Friend, H. Sirringhaus, A general approach for hysteresis-free, operationally stable metal halide perovskite field-effect transistors. *Sci. Adv.* **6**, eaaz4948 (2020).

Downloaded from http://advances.sciencemag.org/ on April 10, 2020

Science Advances

# A general approach for hysteresis-free, operationally stable metal halide perovskite field-effect transistors

Satyaprasad P. Senanayak, Mojtaba Abdi-Jalebi, Varun S. Kamboj, Remington Carey, Ravichandran Shivanna, Tian Tian, Guillaume Schweicher, Junzhan Wang, Nadja Giesbrecht, Daniele Di Nuzzo, Harvey E. Beere, Pablo Docampo, David A. Ritchie, David Fairen-Jimenez, Richard H. Friend and Henning Sirringhaus

*Sci Adv* **6** (15), eaaz4948.
DOI: 10.1126/sciadv.aaz4948

**ARTICLE TOOLS** http://advances.sciencemag.org/content/6/15/eaaz4948

**SUPPLEMENTARY MATERIALS** http://advances.sciencemag.org/content/suppl/2020/04/06/6.15.eaaz4948.DC1

**REFERENCES** This article cites 57 articles, 5 of which you can access for free
http://advances.sciencemag.org/content/6/15/eaaz4948#BIBL

**PERMISSIONS** http://www.sciencemag.org/help/reprints-and-permissions

Downloaded from http://advances.sciencemag.org/ on April 10, 2020

Use of this article is subject to the Terms of Service

*Science Advances* (ISSN 2375-2548) is published by the American Association for the Advancement of Science, 1200 New York Avenue NW, Washington, DC 20005. The title *Science Advances* is a registered trademark of AAAS.

Copyright © 2020 The Authors, some rights reserved; exclusive licensee American Association for the Advancement of Science. No claim to original U.S. Government Works. Distributed under a Creative Commons Attribution NonCommercial License 4.0 (CC BY-NC).